npj | 2D materials and applications

Article

Published in partnership with FCT NOVA with the support of E-MRS

https://doi.org/10.1038/s41699-025-00577-x

WSe_2 nanoflowers grown on $Ti_3C_2Cl_2$ MXene for energy applications and sensing

Antonia Kagkoura ✉, Anastasios Papavasileiou, Shuangying Wei, Filipa. M. Oliveira, Jiří Šturala & Zdeněk Sofer ✉

Developing multifunctional materials for energy and sensing is challenging due to demands for high conductivity, catalytic activity, and structural stability. We report a $WSe_2/Ti_3C_2Cl_2$ hybrid synthesized via one-step solvothermal growth of WSe_2 nanoflowers on Cl-terminated MXene. The strong interface improves electron transport and active site exposure, achieving excellent hydrogen evolution activity with an overpotential of −0.19 V vs RHE at −10 mA cm^{-2}. The WSe_2-rich hybrid delivers an initial discharge capacity of 1255 mAh g^{-1} as a lithium-ion battery anode, outperforming its individual components. MXene boosts conductivity, while WSe_2 morphology buffers volume changes. For sensing, the hybrid doubles the H_2O_2 reduction signal of WSe_2 and enables amperometric detection from 1 to 88 μM with a 0.6 μM detection limit. Overall, in situ growth of WSe_2 on MXene offers a scalable route to efficient multifunctional materials.

Electrochemistry has garnered significant attention in recent years thanks to its unique ability to combine energy storage, conversion, and sensing technologies, serving as a cost-effective alternative for environmental sustainability[1]. The performance of these electrochemical systems relies upon using materials that facilitate electron transfer and enhance the efficiency of the applications. Nevertheless, each electrochemical system has unique requirements that can differentiate the suitability of various materials. High electrical conductivity, good charge transfer kinetics, and large surface area are desirable properties of electrochemical systems[1,2]. In contrast, good adsorption, high (electro)catalytic activity, and porosity are more controversial properties that can benefit one application and interfere with the other. This duality highlights the need for multifunctional materials capable of enhancing several electrochemical processes simultaneously, offering a solution to multiple challenges at once. Recent advances in materials design, especially 2D materials like MXenes and transition metal dichalcogenides (TMDs), have opened new possibilities for electrocatalysis, energy storage, and sensing applications[3,4].

In the field of electrocatalytic hydrogen production, the hydrogen evolution reaction (HER) has gained attention as a promising method for sustainable energy conversion[5,6]. However, the widespread use of noble metal-based electrocatalysts remains hindered by their high cost and limited abundance. Non-precious alternatives, such as MXenes and TMDs, have shown promise as HER electrocatalysts[7–9], though MXenes like Ti_3C_2 have exhibited lower-than-expected HER performance. Despite predictions of high HER activity, Ti_3C_2 MXene has shown a significantly large overpotential in aqueous electrolytes. Specifically, its overpotential is nearly double that of Ti_4N_3 nitride MXene (0.8 V vs. 0.4 V) and is considerably higher than Mo_2C carbide MXene[10]. The reason for this has been recently revealed by studying the electrocatalytic HER mechanism with in situ Raman spectroscopy. The analysis of Ti_3C_2 MXene in the HER process revealed a shift in surface terminations from –O to –OH under acidic conditions, resulting from proton adsorption[11]. This imbalance in protonation and deprotonation at Ti/O sites likely contributes to the high overpotential of Ti_3C_2 MXene during HER. Thus, combining Ti_3C_2 MXene with TMDs, such as tungsten diselenide (WSe_2), is rational to boost their performance[12]. WSe_2 has shown great potential in electrocatalytic HER[8,11,13]. When solvothermal bottom-up methods produce WSe_2, they can provide materials with increased surface area and abundant defected sites that are highly valuable for electrocatalysis and are in high quantity and the desired polymorph. 1T (metallic) phase is more desirable than the semiconducting (2H) due to the sufficient charge transfer that helps the reaction kinetics[9,14].

Lithium-ion batteries (LIBs) continue to be critical in the development of high-performance energy storage solutions, especially for electric vehicles and portable electronics. However, the demand for higher energy density, longer cycle life, and improved rate capability remains a key challenge[15,16]. WSe_2 has shown promise as an anode material due to its high volumetric energy density and efficient lithium-ion diffusion[13,17]. However, its application in batteries has been limited to specific configurations, and further

Department of Inorganic Chemistry, Faculty of Chemical Technology, University of Chemistry and Technology Prague, Technická 5, 166 28 Prague 6, Czech Republic. ✉e-mail: kagkourn@vscht.cz; Zdenek.Sofer@vscht.cz

research is needed to optimize its integration with other materials. In this context, Ti_3C_2 MXene has demonstrated great promise for energy storage[4,18]. Hybridizing MXenes like Ti_3C_2 with TMDs offers an exciting opportunity to combine the high conductivity of MXenes with the electrochemical properties of TMDs to improve battery performance[19].

For sensing applications, particularly in detecting hydrogen peroxide (H_2O_2), advanced materials are needed to improve sensitivity and selectivity. Hydrogen peroxide is crucial in both biological processes and industrial applications, but at high concentrations, it can pose significant health risks[20,21]. Ti_3C_2 MXenes, owing to their excellent electrical conductivity and surface functional groups, have also been actively investigated as promising candidates for electrochemical sensors[22]. As regards sensing, WSe_2 has been involved in gas sensing[23], but its electroanalytical sensing capabilities remain unexplored. Hybrid materials comprising MXenes and TMDs are showing promise for electrochemical sensors[24] due to their unique combination of conductivity and catalytic activity, which is especially beneficial for H_2O_2 detection.

MXenes follow the molecular formula $M_{n+1}X_nT_x$, where M is an early transition metal, A is a group 13 and 14 element, X is carbon and/or nitrogen, and $n = 1–4$. MXenes are synthesized by selective etching of the "A" element of the corresponding MAX phase[25]. This results in a unique 2D material with high conductivity, tunable surface chemistry, and versatility for energy, catalysis, and sensing applications. Over the years, various etching methods have been developed to synthesize MXenes, including traditional hydrofluoric acid (HF)-based etching and, more recently, molten salt (MS).

In this regard, molten salt etching, particularly Lewis acidic molten salt (LAMS) approaches, has emerged as a promising alternative for MXene synthesis due to its ability to produce MXenes with exclusive surface terminations[26]. For example, etching Ti_3AlC_2 MAX phases with molten $CuCl_2$, $FeCl_2$, or $ZnCl_2$ salts has yielded Cl-terminated MXenes. However, these methods are often associated with challenges such as introducing undesired surface groups during post-synthesis washing (e.g., $CuCl_2$ due to washing with ammonium persulfate solution)[26] or the need for inert storage conditions for highly hygroscopic salts like $ZnCl_2$[27]. $CdCl_2$ has also been used as a molten salt for LAMS, yielding high-quality Cl-terminated MXenes[27]. However, its toxicity and carcinogenic risks pose serious concerns for large-scale and sustainable synthesis. We propose the use of potassium chloride (KCl) as a co-solvent to address these limitations and reduce reliance on toxic compounds like $CdCl_2$. It offers practical advantages due to its low cost, wide availability, and ease of handling under ambient conditions. By combining KCl with $CdCl_2$ in optimized ratios, these Cl-terminated MXenes, with their well-defined surface terminations, provide an ideal scaffold for the in situ growth of functional nanomaterials like TMDs.

In situ growth of the immobilization of 2D materials or nanoparticles supported by conductive substrates is a widely recognized concept[28,29]. These substrates provide a structure to support the deposited material and act synergistically to enhance conductivity and charge transfer kinetics. In most electrocatalytic processes, electrical conductivity is one of the most critical factors in achieving good performance. High conductivity can realize very effective energy conversion by reducing the Schottky barrier in the catalyst-electrolyte and catalyst-electrode interfaces, thus facilitating the path that electrons travel and increasing the efficiency of the overall reaction[30]. Existing studies for hybrids consisting of WSe_2 and Mxene are scarce, involving high-temperature synthetic procedures[31], electrostatic interactions[32], or via simple mixing[33]. These hybrids have predominantly been applied to individual applications such as HER and/or supercapacitors[31,34], or gas sensing[32]. However, to the best of our knowledge, the concept of in situ growth of WSe_2 onto Cl-terminated Ti_3C_2 MXene, designed as a truly multifunctional hybrid capable of addressing HER, lithium-ion batteries, and sensing applications, has not been explored. This underscores the potential of our approach in developing a versatile, multifunctional material.

In this work, we employed a straightforward solvothermal method to achieve the in situ growth of WSe_2 nanoflowers on $Ti_3C_2Cl_2$ MXene. First, the MXene was synthesized using the LAMS approach, which combined KCl and $CdCl_2$ to achieve Cl-terminated surfaces. The ratios of WSe_2 to MXene were optimized based on the performance in HER in acidic medium. The hybrid material with the optimal ratio was further explored as an anode for LIBs and an electrocatalyst for the amperometric determination of H_2O_2. The materials were structurally and morphologically characterized by using X-ray diffraction (XRD), Raman spectroscopy, scanning electron microscopy coupled with energy dispersive X-ray spectroscopy (SEM-EDS), and transmission electron microscopy (TEM). The strong interaction between the two components due to their immediate contact along with the synergetic effect between the two materials (i) enhance electron flow enabling lower overpotentials to initiate hydrogen production, (ii) attain a higher initial discharge capacity with improved rate capability and cycling stability, resulting in enhanced LIB performance and (iii) exhibit higher cathodic current in the presence of H_2O_2, leading to an electrochemical sensor with improved sensitivity.

Methods

General

Ti_3AlC_2 MAX phase was purchased from Jinzhou Haixin Metal Materials Co., Ltd (China). All the other chemicals, reagents, and solvents were purchased from Sigma–Aldrich and used without further purification.

Synthesis of $Ti_3C_2Cl_2$ MXene

The Cl-terminated MXenes were synthesized using a modified version of a previously reported procedure[35]. Briefly, Ti_3AlC_2 MAX phase (3 g) was mixed with $CdCl_2$ and KCl in varying molar ratios (1:6:2, 1:5:3, 1:3:5, and 1:2:6). The mixture was homogenized using a mortar and pestle, and ground for 10 min. The resulting mixtures were pressed into pellets and placed in alumina crucibles. The reactions were conducted under an inert argon atmosphere (flow rate ≈4 mL/min) in an alumina tube at 700 °C with a dwell time of 24 h, with a heating and cooling rate of 2 °C/min. After the reaction, the MXenes were recovered by dissolving the residues of cadmium metal in concentrated HCl. For this, the solid products, including the alumina crucible, were transferred to a glass beaker, and 200 mL of HCl was added and left overnight to ensure the complete dissolution of excess reactants. The mixture was then centrifuged (3224 rcf, 5 min) and washed with deionized water until the supernatant reached a neutral pH, followed by two additional washes with methanol. Finally, the sample was vacuum-dried at 35 °C for at least 12 h, and the powder was collected for subsequent steps.

Preparation of WSe_2

Tungsten hexacarbonyl (1 mmol) and selenium powder (2 mmol) were dissolved in 30 mL of dimethylformamide (DMF), and the resulting suspension was transferred into a 50 mL Teflon-lined stainless-steel autoclave reactor and heated at 200 °C for 13 h. After the autoclave was cooled to room temperature, the resulting suspension was centrifuged for 30 min. at 10,000 rpm with DMF (2 times), distilled water (3 times), and methanol (3 times).

Preparation of $WSe_2/Ti_3C_2Cl_2$ MXene with higher WSe_2 content

Tungsten hexacarbonyl (0.5 mmol) and selenium powder (1 mmol), along with 2.5 mg of $Ti_3C_2Cl_2$ MXene, were dissolved in 30 mL DMF, and the resulting suspension was transferred into a 50 mL Teflon-lined stainless-steel autoclave reactor and heated at 200 °C for 13 h. After the autoclave was cooled to room temperature, the resulting suspension was centrifuged at 10,000 rpm with DMF (2 times), distilled water (3 times), and methanol (3 times). This sample is designated as w-$WSe_2/Ti_3C_2Cl_2$.

Preparation of $WSe_2/Ti_3C_2Cl_2$ MXene with higher MXene content

Tungsten hexacarbonyl (0.145 mmol) and selenium powder (0.29 mmol), along with 20 mg of $Ti_3C_2Cl_2$ MXene, were dissolved in 30 mL DMF, and the resulting suspension was transferred into a 50 mL Teflon-lined stainless-

steel autoclave reactor and heated at 200 °C for 13 h. After the autoclave was cooled to room temperature, the resulting suspension was centrifuged at 10,000 rpm with DMF (2 times), distilled water (3 times), and methanol (3 times). This sample is designated as m-$WSe_2/Ti_3C_2Cl_2$.

Microscopy techniques

The morphology of the analyzed materials was investigated using SEM with a Tescan MAIA-3 Field Emission Gun Scanning Electron Microscope (FEG-SEM). EDS measurements were performed for elemental composition and mapping of elements using an 80 mm^2 SDD detector (Oxford Instruments) and AZtecEnergy software from Oxford Instruments. The samples were placed on a carbon conductive tape to conduct the measurements. Transmission electron microscopy (TEM) was performed using an EFTEM Jeol 2200 FS microscope (Jeol, Japan) at an acceleration voltage of 200 keV. Pictures were taken by a SIS MegaView III digital camera (Soft Imaging Systems) and analyzed by AnalySIS v. 2.0 software. Elemental maps were acquired with an SDD detector X-MaxN 80 TS from Oxford Instruments (England). For sample preparation, suspensions were prepared in pure ethanol and drop-cast on a TEM grid (Cu, 200 mesh, Formvar/carbon from TED PELLA, Inc.) and dried overnight at room temperature.

XRD

X-ray powder diffraction data were collected at room temperature on a Bruker D8 Discoverer (Bruker, Germany) powder diffractometer with parafocusing Bragg–Brentano geometry using CuKα radiation (λ = 0.15418 nm, U = 40 kV, I = 40 mA). Data were scanned over the angular range 5–70° (2θ). Data evaluation was performed in the software package EVA.

Raman spectroscopy

InVia Raman microscope (Renishaw, England) in backscattering geometry with a CCD detector was used for Raman spectroscopy. DPSS laser (532 nm, 50 mW) with an applied power of 5 mW and a 50× magnification objective was used for the measurement. Instrument calibration was achieved with a silicon reference, which gives a peak position of 520 cm^{-1} and a resolution of less than 1 cm^{-1}. The samples were suspended in deionized water (1 mg/ml) and ultrasonicated for 10 min. The suspension was deposited on a small piece of silicon wafer and dried.

Electrochemical measurements for the hydrogen evolution reaction

The electrochemical characterization by means of linear sweep voltammetry (LSV) was performed using an Autolab PGSTAT 204 (Metrohm, Switzerland). A standard three-compartment electrochemical cell was used, equipped with an RDE with a glassy carbon disk (geometric surface area: 0.196 cm^2) as a working electrode, a graphite rod as a counter electrode, and $Hg/HgSO_4$ (0.5 M K_2SO_4) as a reference electrode. HER LSV measurements were performed at room temperature in N_2-saturated aqueous 0.5 M H_2SO_4 solution. LSV plots were corrected for iR drop by applying a 5–10% iR correction to the measured potentials to account for the ohmic losses, as the correction varied depending on the resistance of the samples. For preparing the catalyst ink, catalytic powder (4.0 mg) was dissolved in a mixture (1 mL) of deionized water, isopropanol, and 5% Nafion (v/v/v = 4:1:0.02), followed by sonication for 30 min before use. The working electrode was polished with alumina suspension, washed with deionized water, and finally sonicated in double-distilled water before casting 8.5 μL aliquots of the electrocatalytic ink on the electrode's surface. Finally, electrochemical impedance spectroscopy (EIS) measurements were acquired from 10^5 to 10^{-1} Hz with an AC amplitude of 0.01 V. The EIS measurements were conducted at a potential where significant HER current was recorded, corresponding to −2 mA cm^{-2}.

Electrochemical energy storage testing

The slurries were composed of 80 wt.% active material (WSe_2, $Ti_3C_2Cl_2$ MXene, and w-$WSe_2/Ti_3C_2Cl_2$ hybrid), 10 wt.% polyvinylidene fluoride (PVDF) as the binder, and 10 wt.% carbon black (CB) as the conductive additive. These components were thoroughly dispersed in N-methyl-2-pyrrolidone (NMP), which was used as the solvent. To ensure uniform dispersion, the slurry was stirred overnight at room temperature prior to electrode fabrication. The slurry was cast onto planar copper (Cu) foil (7 μm thickness), which served as the current collector. A doctor blade set at a height of 250 μm was employed to ensure uniform coating of the slurry on the Cu foil. The coated electrodes were dried in a vacuum oven at 100 °C for 12 h to remove residual solvent. The dried electrodes were then cut into circular disks and stored in an argon-filled glovebox to prevent exposure to moisture or oxygen before cell assembly. The electrochemical performance of the prepared anodes was evaluated using a two-electrode CR2032 coin cell configuration with metallic lithium (Li) as the counter and reference electrode. The electrolyte consisted of 1 M $LiPF_6$ dissolved in a mixture of ethylene carbonate (EC), diethyl carbonate (DEC), and dimethyl carbonate (DMC) (1:1:1 by volume), with 1 wt.% vinylene carbonate (VC) added as a stabilizing agent. The cells were assembled in an argon atmosphere, ensuring minimal contamination, and then tested for electrochemical performance using a Neware battery testing system. Galvanostatic charge-discharge cycling was performed within a voltage window of 0.001–3.0 V *vs.* Li^+/Li, at an initial current density of 50 mA g^{-1} to evaluate the specific capacities of the anode materials. The rate capability was assessed by cycling the electrodes under varying current densities of 25, 50, 100, 200, and 400 mA g^{-1}, with each current density being maintained for five consecutive cycles. Cyclic voltammetry (CV) and EIS were employed using an Autolab PGSTAT204 workstation (Eco Chemie, Utrecht, Netherlands) to evaluate the electrochemical performance of WSe_2, $Ti_3C_2Cl_2$ MXene, and their hybrid in 2032 coin cells. CV tests were performed at a scan rate of 1.0 mV s^{-1} over a potential range of 0.001–3.0 V vs. Li^+/Li. EIS measurements were conducted at open circuit voltage (OCV) with an AC perturbation of 10 mV over a frequency range from 100 kHz to 100 mHz.

Electrochemical sensing

Measurements were carried out in a 0.1 M phosphate buffer saline (PBS) at pH 7 under ambient conditions, using a 4-channel potentiostat in a three-electrode electrochemical cell. Glassy carbon (GC) electrode was modified with a 10 μL aliquot of 5 mg ml^{-1} ethanolic suspension of the $WSe_2/Ti_3C_2Cl_2$, dried under ambient conditions, and served as the working electrode. Pt foil served as a counter electrode, and Ag/AgCl, 3 M KCl served as a reference electrode. Before every use, the GC electrode was carefully polished with alumina slurry on a polishing pad until a mirror finish was obtained, sonicated in ethanol/water for 7 min, and rinsed thoroughly with distilled water.

CV was measured in a potential range from 0.2 to −0.4 V in the presence of 5 mM H_2O_2 at a scan rate of 25 mV s^{-1}. Amperometry experiments were conducted in stirred (150 rpm) solutions at a polarization potential of −0.3 V, unless stated otherwise.

Discussion

Synthesis of Cl-terminated $Ti_3C_2T_x$ MXene

XRD patterns of the synthesized $Ti_3C_2T_x$ MXene obtained with varying ratios of KCl and $CdCl_2$ (1:6:2, 1:5:3, 1:3:5, and 1:2:6) are presented in Fig. 1a, with the pristine T_3AlC_2 MAX phase included for comparison. The Ti_3AlC_2 MAX phase exhibits characteristic diffraction peaks at 9.52°, 19.11°, and 38.76° 2θ values, typical of its well-defined layered structure (PDF 04-012-0632).

When different ratios of $CdCl_2$ and KCl are employed at 700 °C for 24 h, notable changes in the diffraction patterns (Fig. 1a) are observed. For samples prepared with MAX phase: $CdCl_2$: KCl ratios of 1:6:2, 1:5:3, and 1:3:5, a clear shift of the (002) and (004) diffraction peak positions to lower 2θ values is evident, as indicated by the dotted lines in Fig. 1a, confirming the successful removal of the Al layer and the synthesis of $Ti_3C_2T_x$ MXene. For example, in the MXene synthesized with the ratio 1:3:5, the (002) and (004) diffractions are measured at 7.96 and 15.98°, respectively. The reactions

involved in the synthesis are as follows:

$$Ti_3AlC_2 + 3CdCl_2 \xrightarrow{KCl,\,700\,^\circ C} Ti_3C_2 + 2Cd + AlCl_3$$

$$Ti_3C_2 + 2CdCl_2 \xrightarrow{KCl,\,700\,^\circ C} Ti_3C_2Cl_2 + 2Cd$$

Here, KCl acts as a molten co-solvent, providing stability and homogeneity to facilitate the reaction. After the reaction, residual cadmium metal and other reaction residuals are dissolved in concentrated HCl, and the $Ti_3C_2Cl_2$ MXene is obtained as a powder. For more details on the synthesis, please see the Experimental section.

These results confirm that the ratios 1:6:2, 1:5:3, and 1:3:5 are favorable for synthesizing Cl-terminated $Ti_3C_2T_x$ MXene. Among these, the ratio of 1:3:5 is particularly noteworthy, as it achieves successful MXene synthesis while significantly reducing the amount of toxic $CdCl_2$ used in the etching process. Notably, at least five parts of KCl are required for effective etching, highlighting the potential for optimizing the $CdCl_2$: KCl ratio to achieve safer and more environmentally friendly protocols using the LAMS method without compromising the structural integrity of the MXene. In contrast, the sample synthesized with a 1:2:6 ratio shows no synthesis of MXene, as its XRD pattern retains the characteristic peaks of the T_3AlC_2 MAX phase at 9.49° and 19.08°, indicating incomplete conversion and the presence of other mixed phases.

SEM-EDS characterization was performed for the MXene synthesized with a 1:3:5 ratio to further validate the effectiveness of the optimized ratio. As observed in Fig. 1b, the SEM image reveals a typical accordion-like morphology, characteristic of multilayered $Ti_3C_2T_x$ MXenes, confirming the successful etching of the corresponding MAX phase. The image demonstrates the well-preserved layered structure of the MXene synthesized with the optimized Ti_3AlC_2:$CdCl_2$:KCl ratio. Additionally, this method enables the synthesis of MXene with Cl terminations, as observed in the EDS elemental mapping in Fig. 1c. A uniform distribution of titanium (Ti) and chlorine (Cl) is evident throughout the layered structure, with only minor traces of aluminum (Al) particles present. The uniform distribution of Cl as a surface termination highlights the effectiveness of the 1:3:5 ratio in synthesizing Cl-terminated MXenes. This MXene, synthesized with the 1:3:5 ratio, will be used for the next steps of the study and designated as $Ti_3C_2Cl_2$.

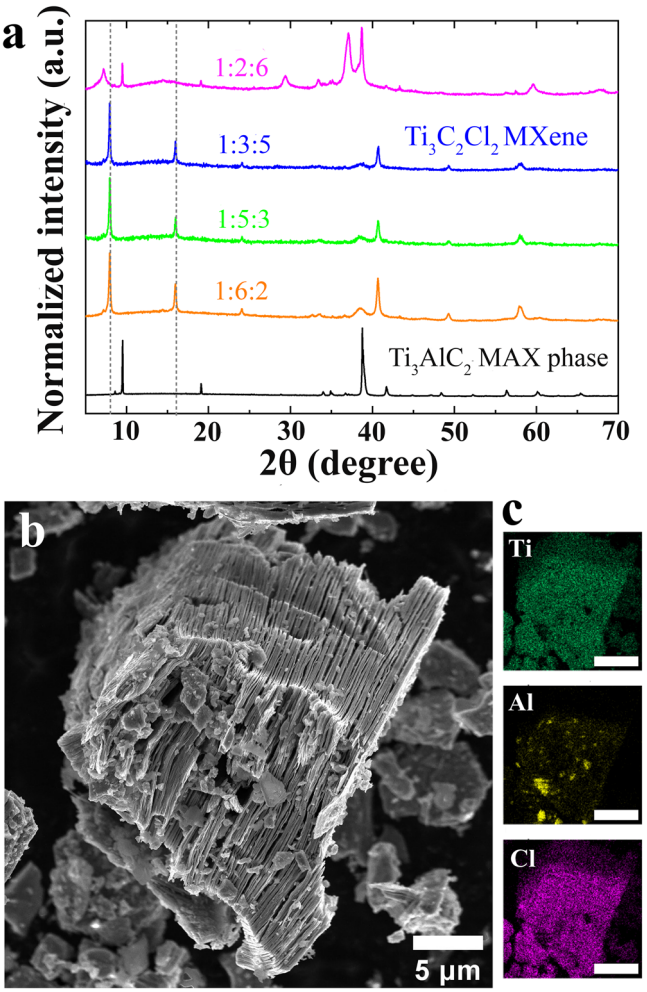

Fig. 1 | Characterization of LAMS-$Ti_3C_2Cl_2$ MXenes. a XRD patterns of MXenes synthesized with different ratios of MAX phase: $CdCl_2$: KCl. **b** SEM image of $Ti_3C_2Cl_2$ MXene synthesized with the optimized ratio of 1:3:5, and **c** corresponding elemental mapping of elements. Scale bars in (**c**) represent 10 μm.

Synthesis of $WSe_2/Ti_3C_2T_x$ MXene hybrids

After the successful synthesis of the $Ti_3C_2Cl_2$ MXene, this study proceeded to the synthesis of the hybrid materials of $WSe_2/Ti_3C_2Cl_2$ MXene with varying compositions: one with a higher ratio of WSe_2 (designated as w-$WSe_2/Ti_3C_2Cl_2$) and the other with a higher ratio of MXene (designated as m-$WSe_2/Ti_3C_2Cl_2$). The hybrid materials were prepared by employing a straightforward solvothermal reaction, in which WSe_2 was deposited onto MXene through the condensation of tungsten hexacarbonyl and selenium. The morphologies of these hybrids are clearly illustrated in the scanning electron microscopy (SEM) images shown in Fig. 2. In the sample m-$WSe_2/Ti_3C_2Cl_2$ (Fig. 2a), the SEM image reveals that the MXene serves as a prominent scaffold, providing a layered structure for the in situ growth of WSe_2 nanoflowers on its surface. The yellow square in Fig. 2a highlights the WSe_2 nanostructures on the $Ti_3C_2Cl_2$ MXene, confirming the formation of the hybrid material. Conversely, the sample w-$WSe_2/Ti_3C_2Cl_2$ (Fig. 2b), exhibits a morphology dominated by WSe_2, with the MXene layers embedded within the WSe_2 matrix. The yellow square in Fig. 2b marks the presence of the $Ti_3C_2Cl_2$ MXene layers embedded by WSe_2.

Additionally, the SEM image of pristine WSe_2 (Fig. 2c) shows a characteristic flower-like morphology, providing an apparent reference for the WSe_2 structure in the hybrids. Figures S1 and S2 provide further EDS

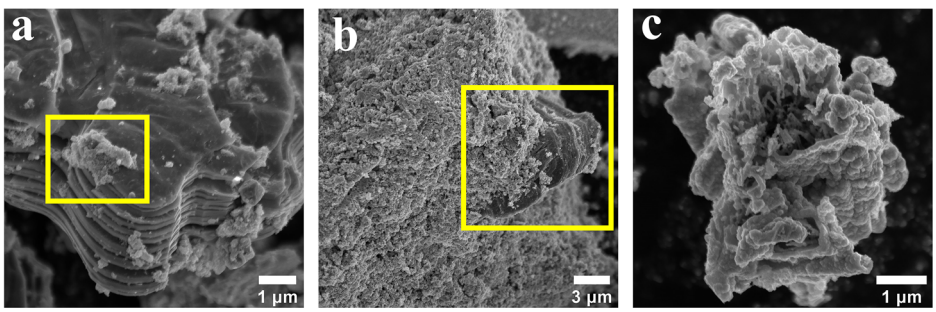

Fig. 2 | Morphology of WSe_2 and hybrid materials. SEM images of (**a**) m-$WSe_2/Ti_3C_2Cl_2$, with the yellow square highlighting WSe_2 onto the $Ti_3C_2Cl_2$ surface. **b** w-$WSe_2/Ti_3C_2Cl_2$, with the yellow square indicating $Ti_3C_2Cl_2$ embedded within the WSe_2. **c** pristine WSe_2.

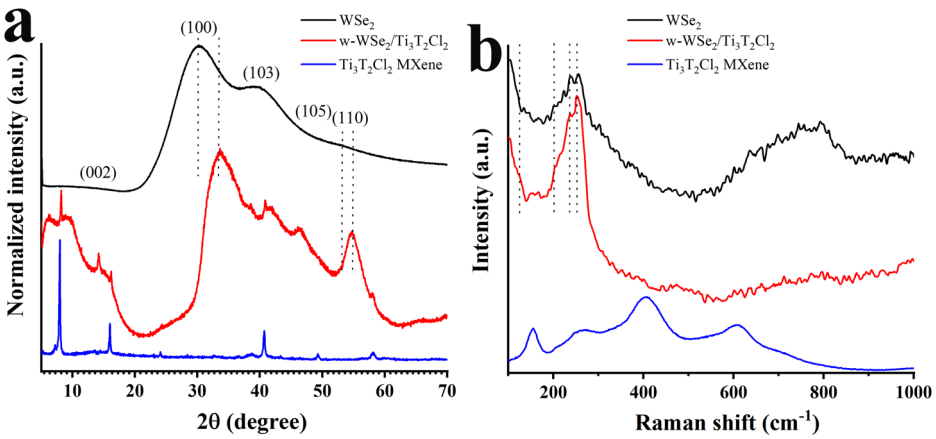

Fig. 3 | Structural and vibrational analysis of pristine and hybrid WSe_2-based materials. a XRD patterns and (**b**) Raman spectra for w-WSe_2/$Ti_3C_2T_2$ MXene (red), WSe_2 (black), and $Ti_3C_2T_2$ MXene (blue).

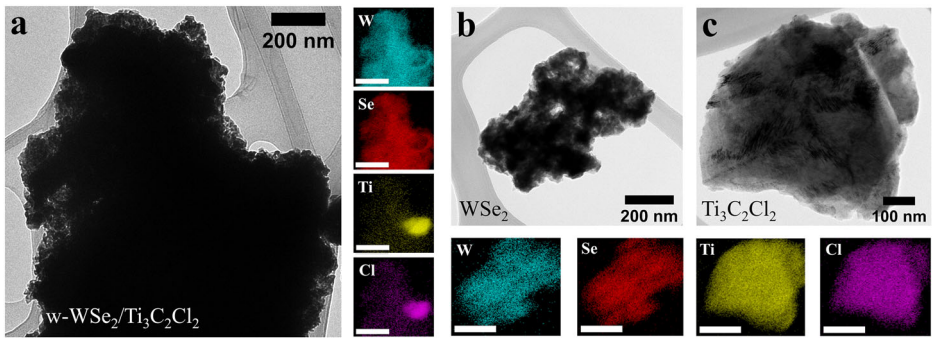

Fig. 4 | TEM characterization of w-WSe_2/$Ti_3C_2Cl_2$ hybrid and starting materials. a TEM image of the w-WSe_2/$Ti_3C_2Cl_2$ hybrid with corresponding EDS elemental maps showing the distribution of W, Se, Ti, and Cl elements; **b** TEM image of WSe_2, with corresponding EDS elemental maps showing the uniform distribution of W and Se; **c** TEM image of $Ti_3C_2Cl_2$ MXene, with corresponding EDS elemental maps showing the uniform distribution of Ti and Cl. Scale bars for mapping in (**a**) represent 500 nm. Scale bars for elemental mapping in (**b**) and (**c**) represent 250 nm.

analysis of individual components, confirming the uniform distribution of elements in the hybrids. Table S1 summarizes the quantification of elements (atomic%) determined by SEM/EDS analysis for all the synthesized materials.

XRD and Raman spectroscopy were employed to characterize the hybrid material. The XRD patterns of w-WSe_2/$Ti_3C_2Cl_2$ MXene further indicate the successful preparation of the hybrid. Figure 3a displays the reflection signals for the plane reflections corresponding to the hexagonal WSe_2 with a P63/mmc space group (reference JCPDF no. 38-1388)[36]. WSe_2 shows (002), (100), (103), (105), and (110) peaks. In the hybrid material (002) and (103) peaks are present while (100) and (110) follow a downward shift of 3.2° and 2.7°, respectively, signifying increased interlayer distance following hybridization[21]. Additionally, peaks at 8.15, 16.16°, 24.34°, 40.89°, 49.02°, and 58.06° originating from the MXene are evident in the hybrid material. All the above confirm the hybrid's successful formation and the interactions between its constituent components. A similar shift is evident in the Raman spectroscopy results. Intact WSe_2 shows bands at 128, 202, and 236 cm^{-1}, corresponding to J_1, J_2, and J_3, which are characteristic of the metallic 1T octahedral phase of WSe_2 (Fig. 3b)[37]. Additionally, the band at 245 cm^{-1} for WSe_2 results from the overlapping $E_2{}^g$ and $A_1{}^g$ modes, typical of the 2H phase[37]. Furthermore, $Ti_3C_2Cl_2$ exhibits characteristic vibrations, including the A_{1g} (Ti, C, O) mode at 206.5 cm^{-1} and broad bands within the 260 and 405 cm^{-1}, attributed to the in-plane (E_g) modes of surface groups attached to Ti atoms[38,39]. In the 580–730 cm^{-1} range, known as the carbon region, a band at 606 cm^{-1} and a shoulder-like band at 704 cm^{-1} correspond to Ti (E_g) and C (A_{1g}) vibrations, respectively[38,39]. In the hybrid material, bands deriving from both individual components are observed: J_1–J_2 bands are seen deriving from WSe_2 are obvious along with the band at 245 cm^{-1}.WSe_2's 256 cm^{-1} band appears downshifted to 253 cm^{-1} in the hybrid. This region also overlaps with the Eg mode associated with Ti atoms in the MXene, indicating strong interfacial coupling between WSe_2 and MXene layers upon hybridization. Also, small bands at 405–606 cm^{-1} are evident[31].

The analysis of the hybrid w-WSe_2/$Ti_3C_2Cl_2$ was further complemented by TEM analysis. Figures 4a and S3 display TEM images of the hybrid, confirming the presence of WSe_2 nanosheets consistent with SEM observations (Fig. 2b). The TEM imaging highlights the flower-like morphology of the WSe_2 nanostructures, formed by interconnected crystalline nanosheets. Furthermore, high-resolution TEM (HRTEM) imaging of the hybrid (Fig. S3) shows well-defined lattice fringes, indicative of its crystalline structure. The corresponding fast Fourier Transform (FFT) patterns of selected areas (insets of Fig. S3) confirm the structural order of the w-WSe_2/$Ti_3C_2Cl_2$. The spatial distribution of elements within the hybrid is shown through STEM-EDS mapping, revealing the integration of $Ti_3C_2Cl_2$ MXene within the WSe_2 nanosheets. In line with the SEM image of the w-WSe_2/$Ti_3C_2Cl_2$ (Fig. 2b), WSe_2 dominates the structure in the hybrid, consistent with its higher ratio in the composition. The EDS mapping (Fig. 4a) confirms the presence and distribution of Ti and Cl elements from the MXene, further supporting the synthesis of the hybrid.

Additionally, the TEM image of pristine WSe_2 (Fig. 4b) highlights its characteristic morphology, and the elemental mapping confirms the uniform distribution of W and Se in the nanosheets. The structural and compositional features of $Ti_3C_2Cl_2$ MXene are presented in Fig. 4c, which illustrates its characteristic layered morphology consistent with the SEM (Fig. 1b). The elemental mapping (Fig. 4f) shows a uniform distribution of Ti and Cl elements, another evidence of the Cl-terminated MXene. TEM analysis of both the hybrid and starting materials (WSe_2 and $Ti_3C_2Cl_2$) aligns well with the SEM-EDS results, providing further evidence of the synthesis of the w-WSe_2/$Ti_3C_2Cl_2$ hybrid by the proposed solvothermal method.

$WSe_2/Ti_3C_2Cl_2$ hybrids as electrocatalysts for HER

Next, the efficacy of both $WSe_2/Ti_3C_2Cl_2$ electrocatalysts and reference materials WSe_2, $Ti_3C_2Cl_2$ MXene, and Pt/C (20 wt.%) for HER was assessed through LSV in an aqueous 0.5 M H_2SO_4 electrolyte (Fig. 5). The hybrid with the higher amount of WSe_2 exhibits excellent electrocatalytic activity, indeed much higher compared to that with the lower amount of WSe_2 (Fig. 5a). w-$WSe_2/Ti_3C_2Cl_2$ starts the production of hydrogen bubbles at −0.14 V vs RHE, 70 and 110 mV lower compared to pristine $Ti_3C_2Cl_2$ MXene and WSe_2, respectively. At the benchmark potential of $-10\ mA\ cm^{-2}$, the w-$WSe_2/Ti_3C_2Cl_2$ hybrid presents an overpotential of just 190 mV, i.e., at −0.19 V vs RHE, 160 mV lower than the m-$WSe_2/Ti_3C_2Cl_2$ and only 159 mV higher than Pt/C. On the contrary, bare $Ti_3C_2Cl_2$ and WSe_2 show much higher overpotentials of 400 and 446 mV, respectively.

The reaction mechanism was analyzed by the extracted Tafel slopes from the LSV curves and by performing Electrochemical impedance spectroscopy (EIS) as seen in Fig. 5b, c, respectively. Consistent with the LSV results, w-$WSe_2/Ti_3C_2Cl_2$ exhibited the lowest Tafel slope value of 50 mV/dec, suggesting that the rate-determining step is the Heyrovsky step. Here, protons undergo initial adsorption onto the electrode surface through a reduction process (Volmer step), followed by molecular H_2 generation, where hydrogen atoms desorb from the electrode (Heyrovsky step). Conversely, m-$WSe_2/Ti_3C_2Cl_2$, along with pristine WSe_2 and $Ti_3C_2Cl_2$, displayed higher Tafel slopes of 144, 186, and 112 mV/dec, respectively, indicating slower reaction kinetics due to proton adsorption. EIS results further support the above findings. Conducted at a potential corresponding to $-2\ mA\ cm^{-2}$ and fitted to a Randles circuit, Nyquist plots showed that w-$WSe_2/Ti_3C_2Cl_2$ had the lowest charge transfer resistance (R_{ct}) at 18.6 Ω, significantly lower than the R_{ct} m-$WSe_2/Ti_3C_2Cl_2$ (141.1 Ω), underscoring the former's superior conductivity. Pristine WSe_2 and $Ti_3C_2Cl_2$ MXene showed higher R_{ct} values of 74.6 and 177.5 Ω, respectively, indicating slower kinetics. The enhanced reaction kinetics of w-$WSe_2/Ti_3C_2Cl_2$, corroborated by Tafel and EIS data, can be attributed to the direct contact enabled by the robust deposition of WSe_2 onto $Ti_3C_2Cl_2$ MXene, facilitating efficient electron transfer within the hybrid structure. Additionally, the abundant flower-like WSe_2 in the hybrid provides a high surface area with more exposed active edge sites for enhanced HER performance. Despite pristine $Ti_3C_2Cl_2$ MXene having higher HER electrocatalytic activity than pristine WSe_2, its lower intrinsic conductivity limits its efficiency. In the w-$WSe_2/Ti_3C_2Cl_2$, WSe_2's superior conductivity and abundant active sites contribute to a more effective HER performance than a $Ti_3C_2Cl_2$ MXene-rich composition.

The electrochemically active surface area (ECSA) is a crucial parameter for understanding charge transport behavior in hybrid materials. ECSA was determined using the equation: $ECSA = C_{dl}/C_s$, where C_{dl} is the electrochemical double-layer capacitance, and C_s represents the specific capacitance for a flat surface of 1 cm^2, assumed to be 40 $\mu F\ cm^{-2}$ for the electrode[13]. To calculate ECSA, cyclic voltammograms of the hybrids, along with WSe_2 and $Ti_3C_2Cl_2$ MXene, were recorded in a non-Faradaic region at scan rates from 50 to 500 $mV\ s^{-1}$ (Fig. S4). The w-$WSe_2/Ti_3C_2Cl_2$ hybrid achieved the highest ECSA value of around 21.7 cm^2, followed by the m-$WSe_2/Ti_3C_2Cl_2$ hybrid with 9.0 cm^2. In comparison, WSe_2 and $Ti_3C_2Cl_2$ MXene showed lower values of approximately 3.6 and 3.1 cm^2, respectively. These findings align with overall electrocatalytic observations, as w-$WSe_2/Ti_3C_2Cl_2$ exhibits abundant active sites and a larger surface area due to the higher presence of WSe_2. Higher ECSA values reflect a greater active surface area of catalytic sites, which is directly linked to improved electrocatalytic performance.

Finally, the stability of both hybrids and the pristine materials was examined by successive scanning of 10,000 electrocatalytic cycles, as presented in Fig. 5a. Notably, both hybrids exhibited a minimal potential loss of only 20 mV, while WSe_2 and $Ti_3C_2Cl_2$ showed a larger overpotential of 40–50 mV. Furthermore, chronoamperometric analysis was conducted at a constant applied potential of −0.16 V vs. RHE for 10,000 with a rotation speed of 1600 rpm (Fig. S5), to further evaluate the durability of w-$WSe_2/Ti_3C_2Cl_2$. w-$WSe_2/Ti_3C_2Cl_2$ exhibited excellent stability with a negligible current density loss of about 11.5%.

These results consequently point out the stability of $WSe_2/Ti_3C_2Cl_2$ hybrids and, in this regard, their potential for long-time applications in demanding electrochemical processes where stability is an important issue for practical use. All tested parameters for HER are summarized in Table S2.

After evaluating the HER performance of all hybrid compositions in a N_2-saturated aqueous 0.5 M H_2SO_4 electrolyte, the hybrid with the optimal $WSe_2/Ti_3C_2Cl_2$ MXene ratio, i.e., with higher WSe_2 content, was identified as the best-performing material due to its high electrocatalytic activity.

Having identified the optimized hybrid, we proceeded to evaluate its potential for additional energy-related and electrochemical applications. Applications like HER, LIBs, and electrochemical sensing rely on efficient electron transfer, high catalytic activity, and structural stability, all of which are intrinsic to the hybrid's design. Specifically, the strong electrocatalytic activity and enhanced electron transfer properties of the optimized hybrid made it a promising candidate for both energy storage as an anode material in LIBs and electrochemical sensing for the amperometric determination of H_2O_2.

w-$WSe_2/Ti_3C_2Cl_2$ MXene hybrid as an anode for LIBs

The electrochemical performance of the w-$WSe_2/Ti_3C_2Cl_2$ hybrid and bare WSe_2 was evaluated. The lithiation of TMDs, such as WS_2, MoS_2, and WSe_2, typically involves a two-step intercalation-conversion mechanism[40]. During lithiation, Li^+ ions intercalate into WSe_2 to form an intermediate Li_xWSe_2 phase, which undergoes a conversion reaction to yield lithium selenide (Li_2Se) and elemental tungsten (W) embedded in the matrix[41]. Conversely, during delithiation, Li_2Se and W recombine to regenerate the Li_xWSe_2 structure, from which Li^+ ions are deintercalated[42]. Galvanostatic charge/discharge tests revealed significant differences in the electrochemical behaviors of the w-$WSe_2/Ti_3C_2Cl_2$ hybrid and bare WSe_2. Voltage profiles recorded at $50\ mA\ g^{-1}$ within a voltage range of 0.001–3.0 V vs. Li^+/Li showed that bare WSe_2 (Fig. 6b) exhibited no discernible plateaus or characteristic features, reflecting sluggish lithiation/delithiation kinetics. Likewise, no prominent lithiation/delithiation peaks were observed for the w-$WSe_2/Ti_3C_2Cl_2$ hybrid (Fig. 6c). While bare WSe_2 exhibited an initial discharge capacity of 661 $mAh\ g^{-1}$, declining to 240 $mAh\ g^{-1}$ after 20 cycles, the w-$WSe_2/Ti_3C_2Cl_2$ hybrid demonstrated a much higher initial discharge capacity of 1255 $mAh\ g^{-1}$. It also retained a similar discharge capacity to WSe_2 of 244 $mAh\ g^{-1}$ after 20 cycles (Fig. 6d). Additionally, intact $Ti_3T_2Cl_2$ MXene shows an initial discharge capacity of 393 $mAh\ g^{-1}$, which decreased to 116 $mAh\ g^{-1}$ after 20 cycles (Fig. 6a). These results highlight the synergistic effect between WSe_2 and $Ti_3C_2Cl_2$ within the hybrid structure, which enhances initial capacity while maintaining stability over cycling.

The rate capability of the hybrid, evaluated under current densities ranging from 25 to 400 $mA\ g^{-1}$ (Fig. 6e),demonstrated superior performance achieving specific capacities of 903, 839, 340, 123, and 50 $mAh\ g^{-1}$ at 25, 50, 100, 200, and 400 $mA\ g^{-1}$, respectively, in contrast to the significantly lower performance of bare WSe_2. The significant enhancement in rate and cycling performance can be attributed to two primary factors: (1) the immediate contact between WSe_2 grown onto the $Ti_3T_2Cl_2$ MXene matrix, enables charge transfer and increases conductivity within the w-$WSe_2/Ti_3C_2Cl_2$, and (2) the unique flower-like morphology of WSe_2 nanostructures, formed by interconnected crystal nanosheets providing better mechanical stability. This architecture ensures the uniform growth of few-layered WSe_2 nanoflowers on $Ti_3C_2Cl_2$ MXene, effectively accommodating volume changes during lithiation/delithiation and preventing mechanical degradation[43,44]. The integration of WSe_2 onto w-$Ti_3C_2Cl_2$ MXene improves electrical conductivity and structural stability, resulting in a commendable electrochemical performance. These findings underscore the w-$WSe_2/Ti_3C_2Cl_2$ hybrid's potential as a promising anode material for advanced lithium-ion batteries.

The Nyquist plots in Fig. S6a were obtained from fresh cells. Among the three samples, the w-$WSe_2/Ti_3C_2Cl_2$ hybrid shows the smallest semicircle, indicating the lowest interfacial resistance and most efficient charge transfer. In contrast, pristine WSe_2 shows a moderate semicircle, while $Ti_3C_2Cl_2$ MXene alone exhibits the largest one, likely due to poor electrolyte

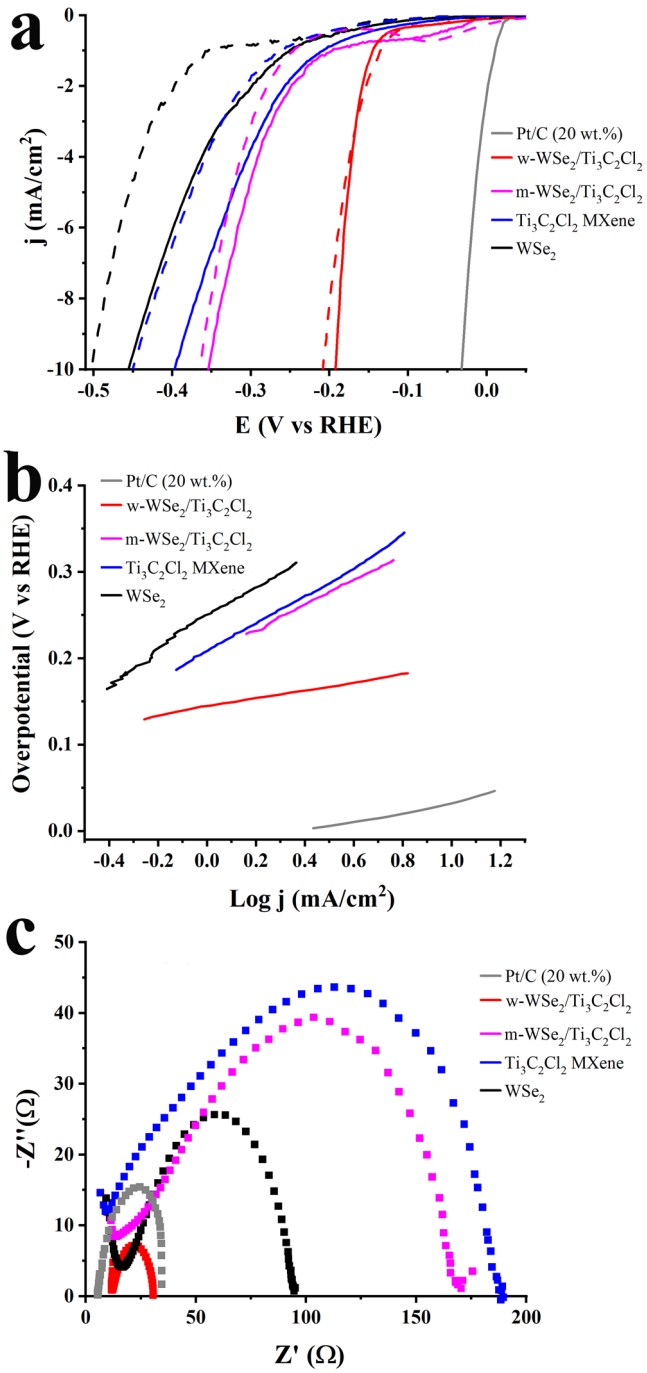

Fig. 5 | Electrochemical evaluation of HER activity and stability in aqueous 0.5 M H_2SO_4. **a** iR- corrected LSVs for HER obtained at 1600 rpm rotation speed and 5 mV s^{-1} scan rate before (solid lines) and after 10,000 cycles (dashed lines), in aqueous (**b**) Tafel slopes, and (**c**) Nyquist plots for w-WSe_2/$Ti_3C_2Cl_2$ (red), m-WSe_2/$Ti_3C_2Cl_2$ (pink), $Ti_3C_2Cl_2$ MXene (blue), WSe_2 (black) and Pt/C (20 wt.%) (gray).

compatibility as a standalone electrode material. While $Ti_3C_2Cl_2$ MXene itself has relatively low conductivity, its integration with WSe_2 in the hybrid structure significantly enhances overall conductivity. These results demonstrate that the hybrid structure exploits the complementary roles of both components. $Ti_3C_2Cl_2$ MXene serves as a structural scaffold that promotes immediate contact and efficient charge transfer, while WSe_2 contributes high Li-ion storage activity,together resulting in enhanced electrochemical performance. The CV peaks of the hybrid electrode show a noticeably higher current response than those of pristine WSe_2, indicating enhanced redox kinetics and faster Li^+ intercalation/deintercalation dynamics enabled by the conductive $Ti_3C_2Cl_2$ MXene framework (Fig. S6b). The $Ti_3C_2Cl_2$ MXene plays a crucial role in enhancing the electrochemical performance by providing a conductive, hydrophilic scaffold that facilitates electrolyte penetration. The direct contact between the MXene scaffold and WSe_2 facilitates more efficient Li^+ transport, improving the interfacial charge transfer and lithium intercalation/deintercalation kinetics. In addition, the w-WSe_2/$Ti_3C_2Cl_2$ hybrid electrode exhibits a significantly reduced peak voltage separation ($\Delta V \approx 720$ mV) compared to pristine WSe_2 ($\Delta V \approx 1350$ mV), indicating lower polarization and improved redox reversibility. Although the ΔV values remain relatively high, which may be attributed to the intrinsic kinetics of layered WSe_2 and interfacial effects, the hybrid structure clearly improves the charge transfer and Li^+ diffusion behavior. This is further corroborated by the increased redox peak currents and closed CV profiles.

w-WSe_2/$Ti_3C_2Cl_2$ hybrid as a sensor for H_2O_2

The sensing features of w-WSe_2/$Ti_3C_2Cl_2$ were investigated and compared with the pristine materials by assessing their electrocatalytic activity towards the reduction of H_2O_2 through CV in the presence of 5 mM in 0.1 M PBS (pH 7) over the potential range from 0.2 to −0.4 V at a scan rate of 25 mV s^{-1}. Results presented in Fig. 7a–d reveal that plain GC shows no response upon the addition of H_2O_2, while the $Ti_3C_2Cl_2$ MXene demonstrates only a negligible current response. On the other hand, both WSe_2 and w-WSe_2/$Ti_3C_2Cl_2$ exhibit a significant increase in cathodic current upon the addition of H_2O_2, with the w-WSe_2/$Ti_3C_2Cl_2$ hybrid displaying nearly double the performance of WSe_2 alone. This is clear evidence that the immediate contact between WSe_2 and $Ti_3C_2Cl_2$ MXene within the hybrid material imparts superior electrocatalytic activity for H_2O_2 reduction, highlighting its capability for enhanced sensing features of this hybrid material.

To this end, the sensing capabilities of w-WSe_2/$Ti_3C_2Cl_2$ were explored using the chronoamperometric technique, correlating the observed catalytic currents with the added concentration of H_2O_2. Aiming to optimize the sensor's experimental conditions, we investigated its behavior at different values of polarization potentials from −0.2 to −0.4 V over a concentration range of 10–100 μM. The amperometric curves in Fig. 7e show that higher potential values increase the current response, while it can affect the stability of the signal. Even though −0.4 V offers higher current responses upon the addition of H_2O_2, it lacks stability and linearity over the selected concentration range. Balancing the need for the highest possible analyte signal with the lowest potential value, and given the comparable performance of the sensor at −0.35 V and −0.30 V, the latter was chosen as the optimal polarization potential.

Later on, the calibration features of the w-WSe_2/$Ti_3C_2Cl_2$ modified GC were assessed through chronoamperometry at an applied potential of −0.3 V. Figure 7f demonstrates the amperometric curve occurred in the presence of H_2O_2 over the concentration range of 1–88 μM. The cathodic current attributed to H_2O_2 addition is linearly correlated with the tested concentration range of H_2O_2 (Fig. 7f inset), with the data fitting the equation ip (μA) = −0.0213[H_2O_2] (μM) − 0.0049 (R^2 = 0.9957). The limit of detection (LOD), calculated as 3σ/slope, was found to be 0.6 μM.

The w-WSe_2/$Ti_3C_2Cl_2$/GC analytical figures-of-merit compare favorably with most of the reported electrochemical sensors for H_2O_2 based on 2D structured materials (Table S3) in terms of LOD and limit of quantification (LOQ). These features, in combination with the relatively low polarization potential along with the absence of the need for any deaeration steps in the working solution, render w-WSe_2/$Ti_3C_2Cl_2$ a highly performing sensing electrocatalyst for H_2O_2.

The reproducibility of the developed sensor was evaluated over five similarly prepared electrodes by addressing the catalytic current stemming from three consecutive additions of 5 μM H_2O_2. Figure 7g illustrates the amperometric curves of the five sensors along with the current response for each of the H_2O_2 additions (Fig. 7g inset). Each one of the three additions in the same sensor causes a -small but dissimilar- dilution to the working solution, resulting in a slightly different concentration of H_2O_2. Considering

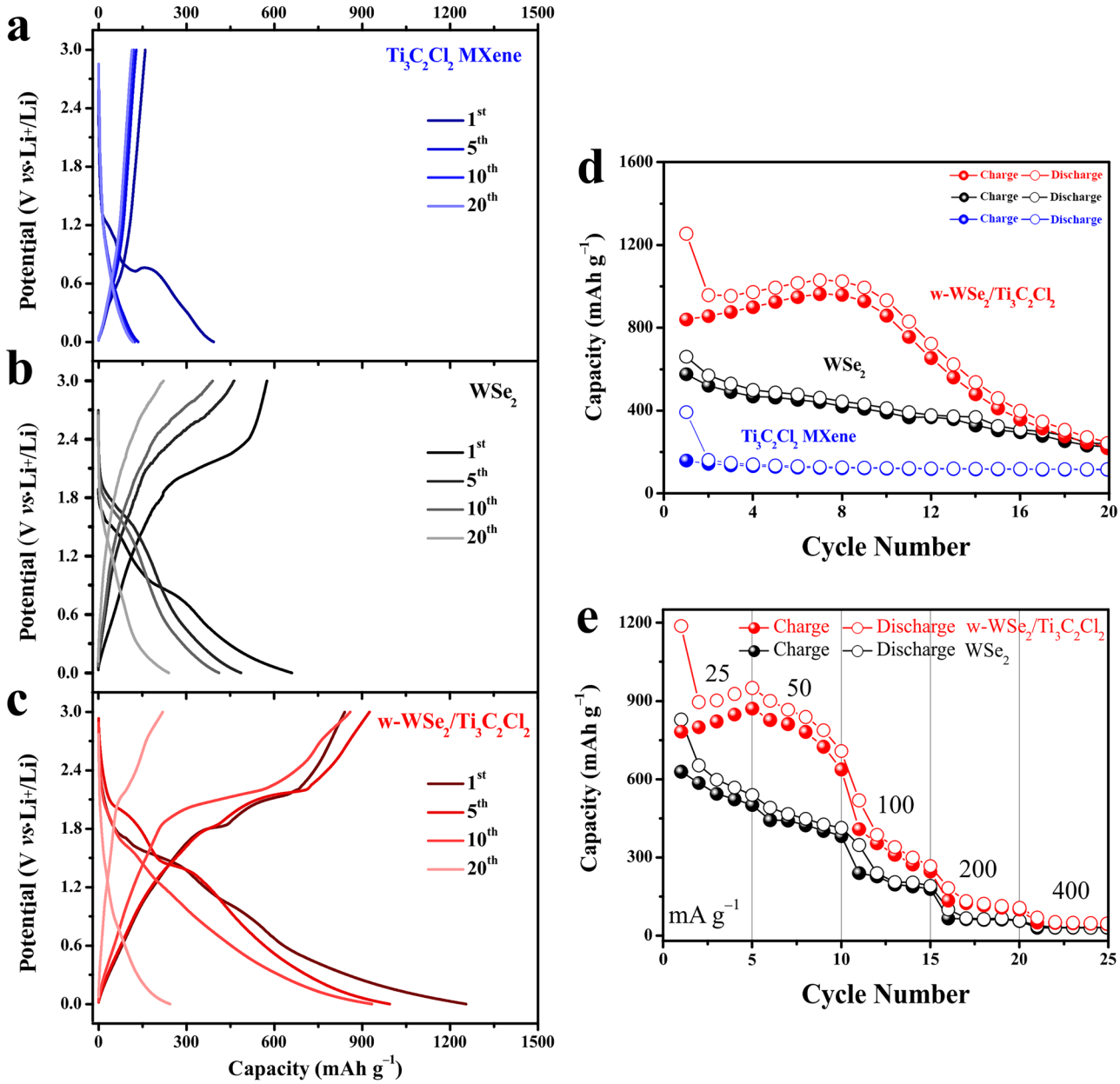

Fig. 6 | Electrochemical evaluation of w-WSe_2/$Ti_3C_2Cl_2$ hybrid, WSe_2, and $Ti_3C_2Cl_2$ MXene in the lithium coin cells. (a) Charge/discharge curves of $Ti_3C_2Cl_2$ MXene at 50 mA g^{-1}. **(b)** Charge/discharge curves of WSe_2 at 50 mA g^{-1}. **(c)** Charge/discharge curves of w-WSe_2/$Ti_3C_2Cl_2$ hybrid at 50 mA g^{-1}. **(d)** Cycling performance comparison of $Ti_3C_2Cl_2$ MXene, WSe_2, and w-WSe_2/$Ti_3C_2Cl_2$ at 50 mA g^{-1}. **(e)** Rate performance comparison of WSe_2 and the w-WSe_2/$Ti_3T_2Cl_2$ under various current densities.

that, the interelectrode relative standard deviation (RSD) was calculated for the three H_2O_2 additions separately, and found to be 7.74%, 8.49%, and 7.87% for the first, second, and third addition, respectively. These values are deemed more than satisfactory and highlight that applying w-WSe_2/$Ti_3C_2Cl_2$ on a GC leads to sensors with fairly good reproducibility over consecutive measurements.

Developing efficient multifunctional materials is essential for tackling energy challenges, environmental safety, and public health concerns. Beyond good performance, a facile fabrication approach is highly desirable. In this context, we developed a hybrid material comprising WSe_2 and $Ti_3C_2Cl_2$ MXene. First, $Ti_3C_2Cl_2$ MXene was synthesized using the LAMS approach, which combined KCl and $CdCl_2$ to achieve Cl-terminated surfaces. This approach not only ensures Cl-terminated MXene surfaces but also minimizes the use of $CdCl_2$, contributing to reduced toxicity. This was followed by a simple solvothermal process, enabling the in situ growth of WSe_2 nanoflowers onto $Ti_3C_2Cl_2$ MXene, forming a well-integrated hybrid material. The hybrid with a higher WSe_2 content exhibited outstanding HER electrocatalytic performance, achieving a low overpotential of just 190 mV at −10 mA cm^{-2}. The strong electronic interaction between WSe_2 and $Ti_3C_2T_2$, facilitated by in situ growth, significantly enhances charge transfer and accelerates reaction kinetics, leading to high HER electrocatalytic activity. Additionally, w-WSe_2/$Ti_3C_2T_2$ demonstrated excellent stability, with only a slight increase in overpotential after 10,000 cycles. After optimizing the WSe_2-to-MXene ratio for HER performance in acidic conditions, we explored its potential in other applications. As an anode material for lithium-ion batteries, w-WSe_2/$Ti_3C_2Cl_2$ exhibited a significantly higher initial discharge capacity of 1255 mAh g^{-1}, nearly twice that of WSe_2 (661 mAh g^{-1}) and more than three times that of $Ti_3C_2T_2$ (394 mAh g^{-1}). It also demonstrated enhanced rate capability and cycling stability. This improvement is attributed to the hybrid's efficient architecture, which

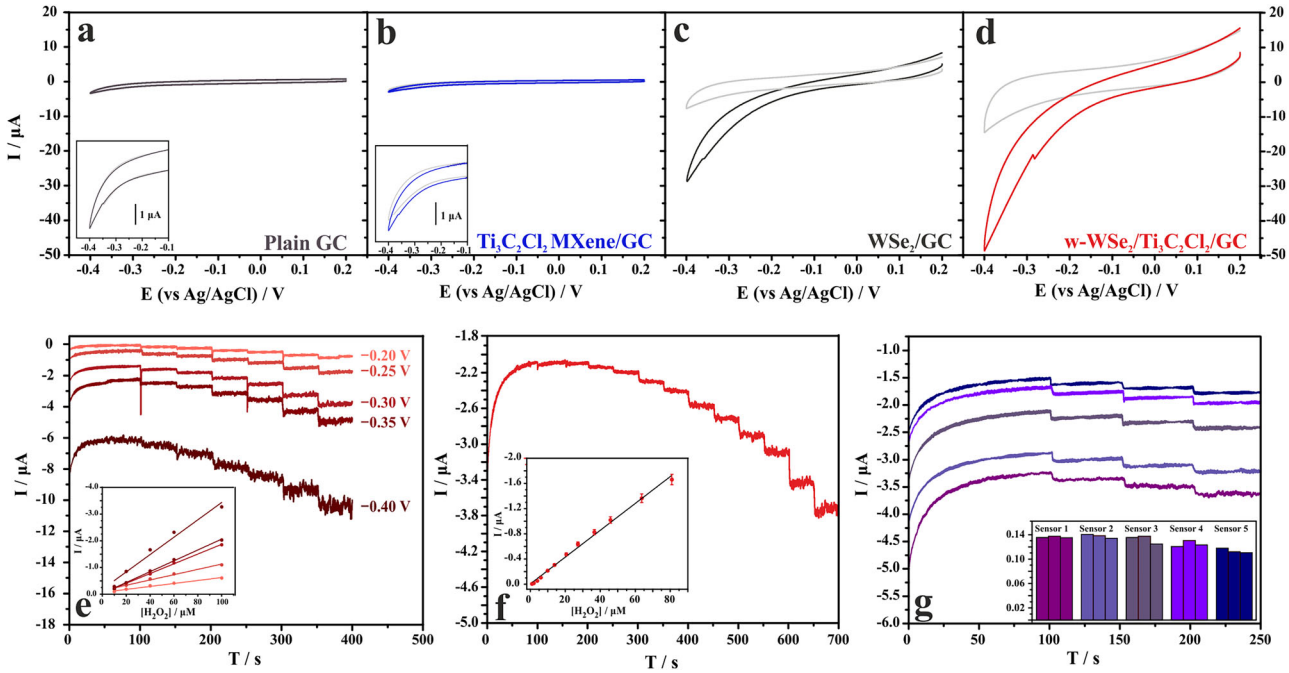

Fig. 7 | Electrochemical sensing of H_2O_2 in 0.1 M PBS (pH 7). a–d CVs of plain GC, $Ti_3C_2Cl_2$ MXene/GC, WSe_2/GC, and w-WSe_2/$Ti_3C_2Cl_2$/GC in the absence and in the presence of 5 mM H_2O_2 at a scan rate of 25 mV s^{-1}. Amperometric curves of w-WSe_2/$Ti_3C_2Cl_2$/GC: **e** at different polarization potentials for H_2O_2 concentration ranging from 10 to 100 μM, along with the respective calibration plots, **f** at −0.3 V for H_2O_2 concentration ranging from 1 to 88 μM along with the corresponding calibration plot, **g** at −0.3 V with similarly prepared sensors over three consecutive additions of 5 μM H_2O_2 along with current response shown for each addition.

promotes charge transfer and conductivity, while the flower-like morphology of WSe_2 accommodates volume changes during lithiation/delithiation and prevents mechanical degradation. Furthermore, the hybrid's architecture,-through the direct contact between its components, offers enhanced sensing capabilities. The w-WSe_2/$Ti_3C_2Cl_2$ hybrid demonstrated superior electrocatalytic activity for H_2O_2 reduction compared to WSe_2 alone. The optimized w-WSe_2/$Ti_3C_2Cl_2$/GC sensor achieved a remarkable sensitivity, with a LOD of 0.6 μM, along with excellent reproducibility, positioning it as a promising electrocatalyst for H_2O_2 sensing. Overall, the development of easily fabricated but highly effective nanomaterials is vital for electrochemical applications, where properties like conductivity, stability, and catalytic activity are essential for promoting electron transfer, electrocatalytic reactions, and energy storage. These insights highlight the promise of the WSe_2/$Ti_3C_2Cl_2$ hybrid as an excellent option for energy-related and sensing applications.

Data availability

The datasets generated during and/or analyzed during the study are accessible via the Zenodo repository: https://doi.org/10.5281/zenodo.14866130.

Received: 15 February 2025; Accepted: 11 June 2025;
Published online: 18 August 2025

References

1. Bard, J. A., Faulkner, L. R. & White, H. S. *Electrochemical Methods: Fundamentals and Applications* (John Wiley & Sons, 2022).
2. Hemanth, N. R. et al. Transition metal dichalcogenide-decorated MXenes: promising hybrid electrodes for energy storage and conversion applications. *Mater. Chem. Front.* **5**, 3298–3321 (2021).
3. Joseph, S. et al. A review of the synthesis, properties, and applications of 2D transition metal dichalcogenides and their heterostructures. *Mater. Chem. Phys.* **297**, 127332 (2023).
4. Kumar, S., Kumari, N. & Seo, Y. MXenes: versatile 2D materials with tailored surface chemistry and diverse applications. *J. Energy Chem.* **90**, 253–293 (2024).
5. Cho, Y. S. & Kang, J. Two-dimensional materials as catalysts, interfaces, and electrodes for an efficient hydrogen evolution reaction. *Nanoscale* **16**, 3936–3950 (2024).
6. Kim, J. H. et al. Engineering active sites of 2D materials for active hydrogen evolution reaction. *Adv. Phys. Res.* **2**, 2200060 (2023).
7. Sheng, M., Bin, X., Yang, Y., Chen, Z. & Que, W. A green and fluorine-free fabrication of 3D self-supporting MXene by combining anodic electrochemical in situ etching with cathodic electrophoretic deposition for electrocatalytic hydrogen evolution. *Adv. Mater. Technol.* **9**, 2301694 (2024).
8. Kagkoura, A. et al. Cobalt- and nickel-doped WSe_2 as efficient electrocatalysts for water splitting and as cathodes in hydrogen evolution reaction proton exchange membrane water electrolysis. *J. Phys. Chem. C.* **129**, 2893–2903 (2025).
9. Yi, L. et al. Tailoring copper single-atoms-stabilized metastable transition-metal-dichalcogenides for sustainable hydrogen production. *Angew. Chem. Int. Ed.* **64**, e202414701 (2025).
10. Johnson, D., Lai, H.-E., Hansen, K., Balbuena, P. B. & Djire, A. Hydrogen evolution reaction mechanism on Ti_3C_2 MXene revealed by in situ/operando Raman spectroelectrochemistry. *Nanoscale* **14**, 5068–5078 (2022).
11. Kwon, I. S. et al. WSe_2–VSe_2 alloyed nanosheets to enhance the catalytic performance of hydrogen evolution reaction. *ACS Nano* **16**, 12569–12579 (2022).
12. Mali, K. H., Pokar, R. & Dashora, A. Origin of surface reconstruction via oxygen termination and improved hydrogen evolution reactions in MXenes. *J. Mater. Chem. A Mater.* **13**, 2859–2874 (2025).
13. Kagkoura, A. et al. Mn-doped WSe_2 as an efficient electrocatalyst for hydrogen production and as anode material for lithium-ion batteries. *Nanoscale* **17**, 947–954 (2025).
14. Song, J. et al. Reaction mechanism and strategy for optimizing the hydrogen evolution reaction on single-layer 1T′ WSe_2 and WTe_2 based on grand canonical potential kinetics. *ACS Appl. Mater. Interfaces* **13**, 55611–55620 (2021).

15. Cui, L. et al. N, P codoped hollow carbon nanospheres decorated with $MoSe_2$ ultrathin nanosheets for efficient potassium-ion storage. *ACS Appl. Mater. Interfaces* **14**, 12551–12561 (2022).
16. Chen, B. et al. Transition metal dichalcogenides for alkali metal ion batteries: engineering strategies at the atomic level. *Energy Environ. Sci.* **13**, 1096–1131 (2020).
17. Zhou, P. et al. Colloidal WSe_2 nanocrystals as anodes for lithium-ion batteries. *Nanoscale* **12**, 22307–22316 (2020).
18. Myint, W. et al. Exploring the electrochemical superiority of V_2O_5/TiO_2@Ti_3C_2-MXene hybrid nanostructures for enhanced lithium-ion battery performance. *ACS Appl. Mater. Interfaces* **16**, 53764–53774 (2024).
19. Ganesan, M. & Lee, J. Y. Layered ion dynamics and enhanced energy storage: VS_2/MXene heterostructure anodes revolutionizing Li-ion batteries. *Nanoscale* **17**, 6039–6048 (2025).
20. Dhara, K. & Mahapatra, D. R. Recent advances in electrochemical nonenzymatic hydrogen peroxide sensors based on nanomaterials: a review. *J. Mater. Sci.* **54**, 12319–12357 (2019).
21. Giaretta, J. E. et al. Flexible sensors for hydrogen peroxide detection: a critical review. *ACS Appl. Mater. Interfaces* **14**, 20491–20505 (2022).
22. Chen, Y. et al. Recent insights on MXene-based architectures for monitoring and sensing of gaseous pollutants: a review. *Talanta* **280**, 126700 (2024).
23. Kumar, A. et al. Strategic review of gas sensing enhancement ways of 2D tungsten disulfide/selenide-based chemiresistive sensors: decoration and composite. *J. Mater. Chem. A Mater.* **12**, 3771–3806 (2024).
24. Kim, S. et al. Three-dimensional MoS_2/MXene heterostructure aerogel for chemical gas sensors with superior sensitivity and stability. *ACS Nano* **17**, 19387–19397 (2023).
25. Naguib, M., Barsoum, M. W. & Gogotsi, Y. Ten years of progress in the synthesis and development of MXenes. *Adv. Mater.* **33**, 2103393 (2021).
26. Li, Y. et al. A general Lewis acidic etching route for preparing MXenes with enhanced electrochemical performance in non-aqueous electrolyte. *Nat. Mater.* **19**, 894–899 (2020).
27. Kamysbayev, V. et al. Covalent surface modifications and superconductivity of two-dimensional metal carbide MXenes. *Science* **369**, 979–983 (2020).
28. Kagkoura, A., Ojeda-Galván, H. J., Quintana, M. & Tagmatarchis, N. Carbon dots strongly immobilized onto carbon nanohorns as non-metal heterostructure with high electrocatalytic activity towards protons reduction in hydrogen evolution reaction. *Small* **19**, 2208285 (2023).
29. Kagkoura, A., Pelaez-Fernandez, M., Arenal, R. & Tagmatarchis, N. Sulfur-doped graphene/transition metal dichalcogenide heterostructured hybrids with electrocatalytic activity toward the hydrogen evolution reaction. *Nanoscale Adv.* **1**, 1489–1496 (2019).
30. Li, G. et al. Engineering substrate interaction to improve hydrogen evolution catalysis of monolayer MoS_2 films beyond Pt. *ACS Nano* **14**, 1707–1714 (2020).
31. Hussain, S. et al. Ultrasonically derived WSe_2 nanostructure embedded MXene hybrid composites for supercapacitors and hydrogen evolution reactions. *Renew. Energy* **185**, 585–597 (2022).
32. Chen, W. Y., Jiang, X., Lai, S.-N., Peroulis, D. & Stanciu, L. Nanohybrids of a MXene and transition metal dichalcogenide for selective detection of volatile organic compounds. *Nat. Commun.* **11**, 1302 (2020).
33. Patel, R. P. et al. Fabrication of a wearable and foldable photodetector based on a WSe_2-MXene 2D–2D heterostructure using a scalable handprint technique. *Nanoscale* **16**, 10011–10029 (2024).
34. Feng, X., Xia, M., Ning, J. & Wang, D. Interface-modified Ti3C2Tx MXene/1T-WSe_2 heterostructure for high-capacitance micro-supercapacitors. *ACS Appl. Energy Mater.* **6**, 6391–6400 (2023).
35. Zhou, C. et al. Hybrid organic–inorganic two-dimensional metal carbide MXenes with amido- and imido-terminated surfaces. *Nat. Chem.* **15**, 1722–1729 (2023).
36. Martínez-Merino, P., Sani, E., Mercatelli, L., Alcántara, R. & Navas, J. WSe_2 nanosheets synthesized by a solvothermal process as advanced nanofluids for thermal solar energy. *ACS Sustain. Chem. Eng.* **8**, 1627–1636 (2020).
37. Park, Y. J. et al. Synthesis of 1T WSe_2 on an oxygen-containing substrate using a single precursor. *ACS Nano* **16**, 11059–11065 (2022).
38. Isailović, J. et al. Study of chitosan-stabilized $Ti_3C_2T_x$ MXene for ultrasensitive and interference-free detection of gaseous H_2O_2. *ACS Appl. Mater. Interfaces* **15**, 31643–31651 (2023).
39. Sarycheva, A. & Gogotsi, Y. Raman spectroscopy analysis of the structure and surface chemistry of $Ti_3C_2T_x$ MXene. *Chem. Mater.* **32**, 3480–3488 (2020).
40. Sun, D. et al. MoS_2/graphene nanosheets from commercial bulky MoS_2 and graphite as anode materials for high rate sodium-ion batteries. *Adv. Energy Mater.* **8**, 1702383 (2018).
41. Wang, X., He, J., Zheng, B., Zhang, W. & Chen, Y. Few-layered WSe_2 in-situ grown on graphene nanosheets as efficient anode for lithium-ion batteries. *Electrochim. Acta* **283**, 1660–1667 (2018).
42. Zheng, X. et al. Preparation and electrochemical performance study of a self-healing electrode composite material with WSe_2/liquid metal Galinstan for lithium-ion batteries. *J. Alloy. Compd.* **969**, 172304 (2023).
43. Kamat, R. S. et al. Oxidized mixed phase $Ti_3C_2T_x$ MXene nanosheets as a high-performance Li-ion battery anode material. *Ionics* **31**, 165–176 (2025).
44. Yang, W., Wang, J., Si, C., Peng, Z. & Zhang, Z. Tungsten diselenide nanoplates as advanced lithium/sodium ion electrode materials with different storage mechanisms. *Nano Res.* **10**, 2584–2598 (2017).

Acknowledgements

A.K. was supported by the Johannes Amos Comenius Programme, European Structural and Investment Funds, project “CHEMFELLS VI” (No. CZ.02.01.01/00/22_010/0008122) from the Ministry of Education, Youth and Sports (MEYS). A.P. was supported by the Onassis Foundation - Scholarship ID: F ZS 045–1/2022–2023 and the Bodossaki Foundation Scholarship. S. W. gratefully acknowledges the financial support from the University of Chemistry and Technology Prague through the Rector’s Junior Grant No. 101852403. F.M.O. thanks the support from the Czech Science Foundation (GA ČR 25-16769S). Z.S. was supported by ERC-CZ program (project LL2101) from Ministry of Education Youth and Sports (MEYS). This work was supported by the project “The Energy Conversion and Storage” funded as project No. CZ.02.01.01/00/22_008/0004617 by Programme Johannes Amos Comenius, call Excellent Research. A.P. was supported by the grant of specific university research – grant No A1_FCHT_2025_013.

Author contributions

A.K. wrote the main manuscript text, synthesis of WSe_2, and electrochemical measurements. A.P. performed electrochemical measurement, S.W. performed battery testing, and F.M.O. and J.S. performed MXene synthesis and their XRD characterization. F.M.O. performed SEM-EDS characterization and TEM data processing. Z.S. supervised work. All authors reviewed the manuscript.

Competing interests

The authors declare no competing interests.

Additional information

Supplementary information The online version contains supplementary material available at https://doi.org/10.1038/s41699-025-00577-x.

Correspondence and requests for materials should be addressed to Antonia Kagkoura or Zdeněk Sofer.